PAPER

Check for updates

Boosting oxygen evolution reaction activity by tailoring MOF-derived hierarchical Co–Ni alloy nanoparticles encapsulated in nitrogen-doped carbon frameworks†

Xiaobin Liu, Xudong Zhao and Li-Zhen Fan [ID] *

The growing demand for sustainable energy has led to in-depth research on hydrogen production from electrolyzed water, where the development of electrocatalysts is a top priority. We here report a controllable strategy for preparing the cobalt–nickel alloy nanoparticles encapsulated in nitrogen-doped porous carbon by annealing a bimetal–organic framework. The delicately tailored hierarchical $Co_2Ni@NC$ nanoparticles effectively realize abundant synergistic active sites and fast mass transfer for the oxygen evolution reaction (OER). Remarkably, the optimized $Co_2Ni@NC$ exhibits a small overpotential of 310 mV to achieve a current density of 10 mA cm^{-2} and an excellent long-term stability in alkaline electrolyte. Furthermore, the underlying synergistic effect mechanism of the Co–Ni model has been pioneeringly elucidated by density functional theory calculations.

1. Introduction

Moving from fossil fuels to renewable energy is undoubtedly the biggest scientific challenge of our time.[1,2] Owing to the pollution free and easy recycling attributes, hydrogen has great potential to be an alternative fuel in the future. Water electrolysis is one of the efficient and promising ways to obtain hydrogen in large quantity.[3,4] Nevertheless, the oxygen evolution reaction (OER) process severely limits the efficiency of overall water splitting because of the sluggish kinetics and large overpotential.[5] Currently, iridium and ruthenium oxides have been proved to be efficient electrocatalysts for OER, but their limited reserves and high costs are great hindrances.[6,7] Despite some progress in recent years, the synthesis of highly-efficient and low-cost non-noble metal alternatives that can compare favorably with noble catalysts remains a challenge.[8,9]

In recent years, some bimetallic alloys (*e.g.*, FeCo, FeNi, and CoNi) have been demonstrated to possess better electrocatalytic activities than their individual entities for OER, because the combination of two metals can form inherent polarity to introduce synergetic effects.[10–12] Among them, CoNi alloy stands out on account of their features of low cost and good environmental friendliness.[13] According to the previous reports, in an alkaline solution, nickel is more likely to desorb OH$^-$ than cobalt, and cobalt is more helpful in increasing the activity of

the Tafel step.[14] In addition, since the freedom degree of Co–Ni alloy is greater than that of pure metal, more opportunities can be provided to optimize the catalytic activity by regulating the proportion of the metal in the alloy.[9,15] However, rational design and controlled synthesis of homogeneous CoNi alloy catalyst with high-activity is still a big challenge: (1) the synthesis process of the porous hierarchical or micro–nano structure is complex and tedious; (2) precise control of multiple phases produced by two metal centers is difficult to achieve; (3) the heteroatoms (N, P, S) are usually doped into carbon to enrich active sites through an additional step, which tends to trigger agglomeration and non-uniform distribution of the active material after the carbonization treatment, resulting in unevenness and inadequate exposure of active sites. To address these problems, the development of a general manufacturing strategy to achieve better catalytic performance is highly desired.

Metal–organic frameworks (MOFs), a family of ordered porous materials consisting of metal center nods and organic ligand linkers, have been proved to be an ideal template to fabricate high-efficiency electrocatalysts.[16,17] On one hand, by using the guiding effect of coordination bond, the MOF structure with uniform size and controllable morphology can be constructed efficiently. After pyrolysis in an inert atmosphere, shrinkage and reconstruction are performed based on the MOF precursor to form the hierarchical nanostructures, which provide large surface area and facilitate fast mass transfer. On the other hand, benefiting from the good compatibility of MOF with various metal ions, the synthesis of homogeneous bimetallic MOF precursors is achievable, leading to the highly uniform dispersion of active sites in atomic level.[18] Apart from

Beijing Advanced Innovation Center for Materials Genome Engineering, Institute of Advanced Materials and Technology, University of Science and Technology Beijing, Beijing 100083, China. E-mail: fanlizhen@ustb.edu.cn

the controllable morphology and compatible metal ions, the as-prepared N-containing bimetal MOFs offer the opportunity to fabricate active materials coated by N-doped carbon (NC) without additional nitrogen source.[19] Bearing these in mind, we develop a controllable synthesis strategy for the construction of cobalt–nickel alloy nanoparticles *via* annealing bimetallic MOF precursors in argon. The optimized $Co_2Ni@NC$ integrates the nanostructure engineering and component modulation together, realizing abundant synergistic active sites and fast mass transfer towards high-activity OER. As a result, it requires a small overpotential of 310 mV to achieve a current density of 10 mA cm^{-2} and exhibits an excellent durability in alkaline electrolyte.

2. Experimental

2.1. Chemicals

Nickel(II) nitrate hexahydrate (Ni(NO$_3$)$_2$·6H$_2$O, 98%), cobalt(II) nitrate hexahydrate (Co(NO$_3$)$_2$·6H$_2$O, 98.5%), 1,4-benzenedicarboxylic acid (H$_2$BDC, 99%), 4,4′-bipyridine (4,4′-bipy, 98%), sodium hydroxide (NaOH, 96%) were purchased from Sinopharm Chemical Reagent Co. Ltd (Shanghai, China). Commercial iridium oxide (IrO$_2$, 99.9%) was purchased from Aladdin (Shanghai, China). Nafion (5 wt%) was purchased from Sigma-Aldrich (Beijing, China). The water for experiments was deionized (DI) water (18 MΩ). Other chemicals and solvents used in this work were obtained from commercial suppliers and used without further purification.

2.2. Materials synthesis

2.2.1. Preparation of Co$_x$Ni$_y$-MOF. Co(NO$_3$)$_2$·6H$_2$O (0.5 mmol), H$_2$BDC (1 mmol), 4,4′-bipy (1 mmol) and NaOH (2 mmol) were dissolved in 50 mL distilled water. The above-mentioned reactants were added to a 100 mL Teflon-lined stainless-steel autoclave and kept at 200 °C for 24 h. After naturally cooled to room temperature, the brown precipitates were collected by centrifugation. Then washed for three times with ethanol and finally dried in a vacuum oven at 60 °C overnight to obtain the Co-MOF. Similarly, Ni-MOF was prepared except that Ni(NO$_3$)$_2$·6H$_2$O (0.5 mmol) was used as the metal source, and Co$_x$Ni$_y$-MOF was synthesized using Co(NO$_3$)$_2$·6H$_2$O and Ni(NO$_3$)$_2$·6H$_2$O as the metal sources with a mole ratio of 2 : 1, 1 : 1 and 1 : 2, named as Co$_2$Ni-MOF, CoNi-MOF and CoNi$_2$-MOF, respectively.

2.2.2. Preparation of Co$_x$Ni$_y$@NC. In a typical procedure, the as-prepared Co-MOF, Ni-MOF and Co$_x$Ni$_y$-MOF were placed in a tube furnace and heated to 300 °C for 1 h under an argon flow. Then the temperature was increased to 800 °C for 2 h with a heating rate of 2 °C min^{-1}. After naturally cooled to ambient temperature, the final black powder was collected.

2.2.3. Preparation of Co$_2$Ni@NC-T. The as-prepared Co$_2$Ni-MOF were placed in a tube furnace and heated to 300 °C for 1 h, then the temperature was increased to 600, 700, 900 and 1000 °C for 2 h with a heating rate of 2 °C min^{-1} under an argon flow, named as Co$_2$Ni@NC-600, Co$_2$Ni@NC-700, Co$_2$Ni@NC-900 and Co$_2$Ni@NC-1000, respectively.

2.3. Materials characterizations

The morphology feature was analyzed by scanning electron microscopy (SEM, JEOL JSM-6330 and QUANTA FEG 450) and transmission electron microscopy (TEM, JEM-2010F). The chemical composition was characterized by energy dispersive spectrometer (EDS) attached to QUANTA FEG 450. The phase composition was characterized by powder X-ray diffraction (PXRD, Rigaku D/max-RB). X-ray photoelectron spectra (XPS) were collected by EscaLab 250Xi Instrument. Raman spectrum was tested by LabRAM HR Evolution. Nitrogen adsorption–desorption measurement was conducted at 77 K with an autosorb iQ automated gas sorption analyzer (Micromeritics ASAP 2460).

2.4. Preparation of working electrode

A glassy carbon (GC) electrode (3 mm in diameter, surface area = 0.07065 cm^2) was used as the working electrode. Typically, 5 mg sample was dispersed in a solution containing 450 μL ethanol, 500 μL deionized water and 50 μL Nafion solution by sonication for 1 hour to form a homogeneous ink. Then, 5 μL well-dispersed catalysts was loaded onto a GC electrode and dried at room temperature.

2.5. Electrochemical measurements

Electrochemical measurements were performed in a three-electrode setup at room temperature using an electrochemical workstation (CHI 660C). A Ag/AgCl (KCl saturated) electrode and a graphite rod were as the reference electrode and the counter electrode, respectively, and 1.0 M KOH was used as the electrolyte. The catalyst was cycled 50 times by CV until a stable CV curve was obtained before testing. Potentials were referenced to a reversible hydrogen electrode (RHE): $E_{RHE} = E_{Ag/AgCl}$ + 0.197 + 0.059 pH. The overpotential (η) was calculated according to the following formula: $\eta = E_{RHE} - 1.23$ V. Linear sweep voltammetry (LSV) was recorded at a scan rate of 5 mV s^{-1} to obtain the polarization curves. EIS was performed at a given potential with frequency from 0.1 to 100 000 Hz. Long-term stability tests were conducted by continuous cyclic voltammetry scans with a sweep rate of 100 mV s^{-1}, and time dependent current density curves tested by chronopotentiometry method at overpotential of 310 mV *vs.* RHE. The electrochemically active surface areas (ECSAs) are usually tested from the electrochemical double-layer capacitance (C_{dl}) by collecting cyclic voltammograms (CVs). The C_{dl} was estimated from cyclic voltammograms measured in a non-faradaic region at different scan rates (20, 40, 60 and 80 mV s^{-1}) in the potential range from 0.94–1.04 V *vs.* RHE. C_{dl} values were evaluated using the equation as follows: $C_{dl} = I_c/\nu$, where C_{dl} is the double-layer capacitance (mF cm^{-2}), I_c is the charging current (mA cm^{-2}), ν is the scan rate (mV s^{-1}).

2.6. Computational details

The projector augmented wave (PAW) method[20] and Perdew, Burke, and Ernzerhof (PBE) functional[21] were adopted in the Vienna *ab initio* simulation package (VASP).[22–24] The energy

cutoff was set to 500 eV ($8 \times 8 \times 1$) Monkhorst–Pack scheme k-point mesh were generated for (111) surface. The convergence energy threshold for the electronic self-consistent loop was set to 10^{-5} eV, while that for the force convergence tolerance was set to 0.01 eV $Å^{-1}$. DFT-D3 method[25] was employed to deal with the weak vdW force between adsorbate and (111) surface. Spin polarization was considered in all computations. The free energy diagrams of the OER were calculated according to the method developed by Nørskov:[26]

$$\Delta G = \Delta E + \Delta E_{ZPE} - T\Delta S + \Delta G_U + \Delta G_{pH}$$

where ΔE stands the energy obtained by DFT simulation, ΔE_{ZPE} is the zero-point energy correction, T is 298.15 K, and ΔS is the entropy change. $\Delta G_U = -eU$, U is the electrode potential and is taken as 0 in this work. $\Delta G_{pH} = -k_B T \ln 10 \times pH$ and pH = 14 was considered. The free energy of gas H_2O at 0.035 bar was used as that of the liquid H_2O at 298.15 K. The free energy of O_2 was obtained from the free energy change of the reaction $O_2 + 2H_2 \rightarrow 2H_2O$, which is -4.92 eV at 298.15 K.

For the OER overpotentials, a method developed by Nørskov was applied:[27]

$$\eta = \frac{\max(\Delta G_1, \Delta G_2, \Delta G_3, \Delta G_4)}{e} - U$$

where $U = 1.23 - k_B T \ln 10 \times pH$.

3. Results and discussion

The preparation process of hierarchical Co$_2$Ni@NC nano-particles is displayed in Fig. 1. In a typical experiment, the CoNi-based bimetallic MOF (denoted as Co$_x$Ni$_y$-MOF), was synthesized with $Co(NO_3)_2 \cdot 6H_2O$, $Ni(NO_3)_2 \cdot 6H_2O$, 1,4-benzenedicarboxylic acid (H_2BDC) and 4,4′-bipyridine (4,4′-bipy). The similar ionic radius and coordination mode of cobalt and nickel ions enable them to be homogeneously incorporated into the Co$_x$Ni$_y$-MOF framework. As shown in Fig. 2a, each metal center contains x Co(II) and y ($y = 1 - x$) Ni(II) cations, which coordinate with two oxygen atoms from one H_2BDC and two nitrogen atoms from two 4,4′-bipy ligands, to form a distorted octahedral geometry. By adjusting the concentrations of cobalt nitrate and

nickel nitrate in the reactants, Co/Ni atom molar ratio in Co$_x$Ni$_y$-MOF can be accurately controlled. X-ray diffraction (XRD) pattern suggests that the as-prepared Co$_x$Ni$_y$-MOFs have very alike diffraction peaks and all can coincide well with the simulated CoNi-MOF (Fig. 2b).[28] The obvious color change from brown to green further illustrates the structure transformation of heterogeneous isomorphism from Co-MOF to Ni-MOF.[29] It can be clearly observed that the as-synthesized Co$_2$Ni-MOF has micron-sized rod-like framework with well-defined smooth surfaces (Fig. S1†). Subsequently, plentiful N-doped carbon coated nanoparticles were gained based on the original rod-like framework after the annealing treatment, resulting in the well-designed hierarchical Co$_2$Ni@NC architectures (Fig. 2c and d). The SEM energy dispersive spectrometer (EDS) mapping images indicate that the elements of Co, Ni, C and N are uniformly distributed in the Co$_2$Ni@NC (Fig. 2e). Transmission electron microscopy (TEM) images further verify that the Co–Ni alloy nanoparticles with N-doped carbon coating are homogenously inlaid into a rod-like framework (Fig. 2f and g). From the high-resolution transmission electron microscopy (HRTEM) image in Fig. 2h, the clear crystal lattice fringes with a spacing of 0.207 nm correspond to the (111) plane of Co (0.2046 nm, JCPDS card no. 15-0806) and Ni (0.2034 nm, JCPDS card no. 65-2865).[13] The selected-area electron diffraction (SAED) pattern displays bright rings corresponding to the (111) and (220) planes of Co and Ni, further proving the polycrystalline character of Co$_2$Ni@NC (Fig. 2i).[30] Additionally, Co$_2$Ni@NC-T (T = 600, 700, 900 and 1000 °C) samples derived from Co$_2$Ni-MOF were prepared to investigate the effect of annealing temperature. The SEM images of Co$_x$Ni$_y$@NC and Co$_2$Ni@NC-T samples with similar morphology are shown in Fig. S2 and S3.†
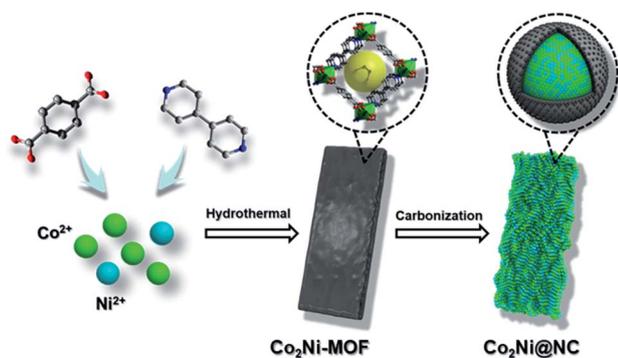

Fig. 1 Schematic illustration of the preparation process of hierarchical Co$_2$Ni@NC nanoparticles derived from bimetal–organic framework with boosting OER activity.
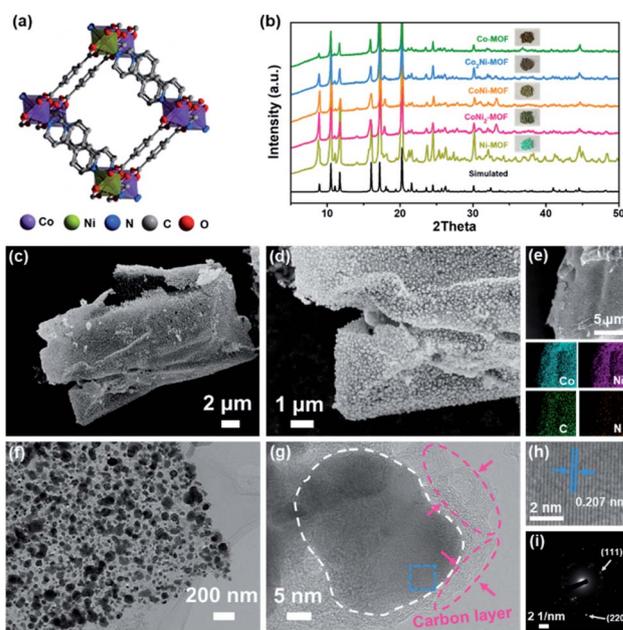

Fig. 2 (a) The crystal structure and (b) XRD patterns of Co$_x$Ni$_y$-MOF. (c and d) SEM, (e) EDS element mapping (Co, Ni, C and N), (f and g) TEM, (h) HRTEM images and (i) SAED pattern of Co$_2$Ni@NC.

The phase characteristics of Co_xNi_y@NC are determined by XRD patterns (Fig. 3a). Each cobalt or nickel metal atom has a coordination number of twelve, showing a face-centered cubic stack geometry (Fig. S4†). The diffraction peaks of Ni@NC positioned at 44.5, 51.8, and 76.4° are attributed to the (111), (200), and (220) planes of Ni (JCPDS card no. 65-2865), respectively. As the Co/Ni molar ratio increases, the metallic Co (JCPDS card no. 15-0806) is finally obtained.[31] During this process, the diffraction peak of the (220) plane shifts from 76.4 to 75.8°, indicating the formation of Co–Ni alloy. Fig. S5† exhibits the XRD patterns of the Co_2Ni@NC-T samples, similar diffraction characteristics to those of the Co_2Ni@NC can be observed. The porous feature of Co_2Ni@NC was estimated by Brunauer–Emmett–Teller (BET) measurement (Fig. S6†). The specific area is 236.6 $m^2\ g^{-1}$ and the average pore-size distribution is concentrated at 8.31 nm. The hierarchical porosity of Co_2Ni@NC with high surface area guarantees fast electron transfer and affords sufficient active sites for oxygen evolution. X-ray photoelectron spectroscopy (XPS) measurements were used to investigate the chemical constitutions and valence states of the Ni@NC, Co_2Ni@NC and Co@NC catalysts. Peaks corresponding to Co, Ni, N, C and O can be clearly observed in the full spectra shown in Fig. S7.†

High-resolution Co 2p XPS spectrum of Co_2Ni@NC is displayed in Fig. 3b. Three important Co-related species including metallic Co, Co–O and Co–N_x are fitted and analyzed. Two pairs of peaks at 778.5/793.8 eV and 780.2/796.6 eV are assigned to the $2p_{3/2}/2p_{1/2}$ doublets of metallic Co and Co–O bond, respectively.[32] Similar to the Co species, metallic Ni, Ni–O and Ni–N_x signals are characterized in the Ni 2p spectrum of Co_2Ni@NC (Fig. 3c). Two pairs of peaks at 853.0/870.4 eV and 856.3/874.4 eV are ascribed to the $2p_{3/2}/2p_{1/2}$ doublets of metallic Ni and Ni–O bond, respectively.[33] Additionally, two pairs of peaks at 785.9/802.7 and 860.6/880.8 eV are fitted to be satellites due to the shakeup excitation of Co^{2+} and Ni^{2+}, respectively.[32,33] The

peaks at 782.2 and 854.3 eV indicate the presence of Co–N_x/Ni–N_x, which has been identified as one of the best active sites for OER.[34,35] For Co_2Ni@NC, owing to the enhanced electron transfer and strong interactions between Co and Ni, the binding energy of metallic Co exhibits a 0.39 eV positive shift compares to Co@NC, while the binding energy of Ni–N_x exhibits a 0.26 eV negative shift in comparison with Ni@NC.[36] N 1s spectrum of Co_2Ni@NC can be fitted into five peaks at 398.4, 399.1, 400.5, 401.3 and 402.4 eV, which are attributed to the pyridinic N, Co–N_x, pyrrolic N, graphitic N and oxidized N, respectively (Fig. 3d).[19] According to the area percentages of the above five peaks, the content percentages of the five nitrogen types are 11.3%, 14.2%, 26.1%, 24.1% and 24.3%, respectively. It is well known that doping graphitic N atoms can offer p-electrons to the π-conjugated sp^2 carbon system, thus enhancing the electronic conductivity of nanostructures. At the same time, the pyridinic-N and pyrrolic-N can create some defects in the nanostructures, promoting the fast mass transfer.[37] In addition, the observation of Co–N_x bond demonstrates that the Co atoms are indeed doped into carbon structure and bonded with the nitrogen. The C 1s peak of Co_2Ni@NC can be deconvoluted into four peaks located at 284.6, 285.2, 286.3, and 289.9 eV, relating to the C=C, C=N, C–O, and C=O bonds, respectively (Fig. S8a†).[38] The presence of C=N bond verifies the formation of N-doped carbon coating, which is favorable to improve the inherent electronic conductivity of materials.[19] The O element from carboxy group may be also a good source to form O doping in carbon for improving electrocatalytic activity (Fig. S8b†).[39] Raman spectrum was used to further confirm the carbon types of Co_2Ni@NC (Fig. S9†). Two peaks at 1340 and 1581 cm^{-1} are ascribed to the sp^2-type D band and G band, respectively. The other two peaks locate at 1065 and 1496 cm^{-1} are indexed to the sp^3-type carbon. By calculation, the intensity ratio of the D-band to the G-band (I_D/I_G) is 0.98, indicating the high degree of graphitization. The intact area ratio of sp^3 to sp^2 (Asp^3/Asp^2) is 65.7%, which suggests a high sp^2-type carbon content for the high electronic conductivity.[40]

The electrocatalytic activities of a series of Co_xNi_y@NC samples for OER were investigated utilizing a typical three-electrode system in alkaline electrolyte (1.0 M KOH). Fig. 4a exhibits the linear sweep voltammetry (LSV) profiles of Co_xNi_y@NC. For comparison, the commercial IrO_2 catalyst was also tested. It is worth mentioning that Co_2Ni@NC reveals the best catalytic performance and the increase or decrease of Co doping content will affect the performance of OER. By precisely adjusting the Co–Ni ratio in the alloy, the charge transfer between the catalyst metal atoms can be accelerated, and a stronger synergy between the two metal centers can be achieved, thereby improving the performance of OER.[9,36] As shown in Fig. 4b, the Co_2Ni@NC could achieve a current density of 10 mA cm^{-2} at an overpotential of 310 mV, the overpotential is lower than those of other Co_xNi_y@NC samples, even better than the commercial IrO_2 (340 mV). The electrocatalytic kinetics of Co_xNi_y@NC for OER were studied by related Tafel plots. In Fig. 4c, the Co_2Ni@NC has a much smaller overpotential of 60.8 mV dec^{-1} than that of IrO_2 (93.9 mV dec^{-1}) and those of other Co_xNi_y@NC samples. These results are superior to that of
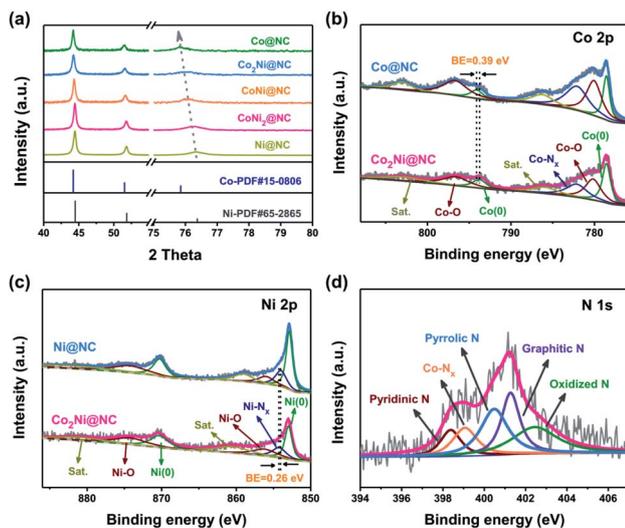

Fig. 3 (a) XRD patterns of Co_xNi_y@NC. High-resolution XPS spectra of (b) Co 2p in Co@NC and Co_2Ni@NC, (c) Ni 2p in Ni@NC and Co_2-Ni@NC, and (d) N 1s in Co_2Ni@NC.
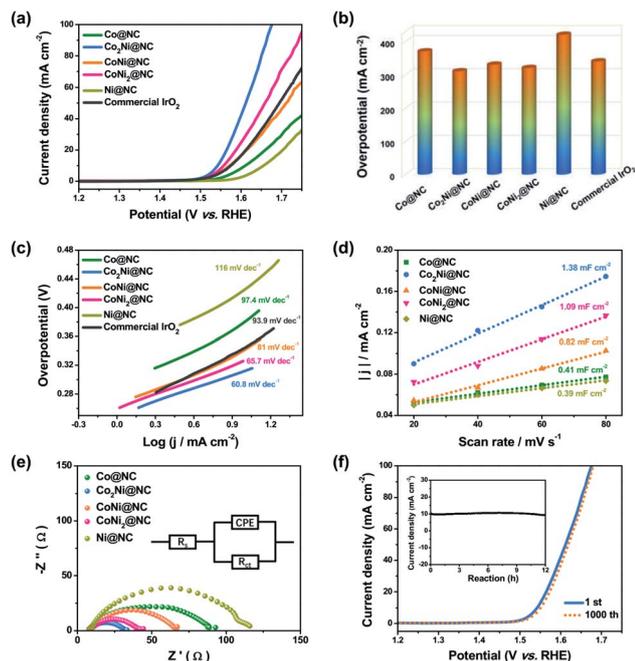
Fig. 4 (a) The OER LSV curves, (b) overpotentials, and (c) Tafel plots of Co@NC, Co$_2$Ni@NC, CoNi@NC, CoNi$_2$@NC, Ni@NC and commercial IrO$_2$. (d) The capacitive currents as a function of scan rates, (e) EIS spectra of Co@NC, Co$_2$Ni@NC, CoNi@NC, CoNi$_2$@NC and Ni@NC. (f) The LSV curves of Co$_2$Ni@NC at the initial state and after 1000 CV cycles. The inset was the chronoamperometric curve.
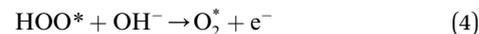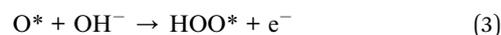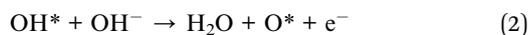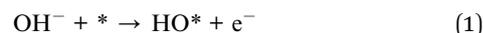
many reported Co-based OER catalysts in basic condition (as is summarized in Table S1†). In addition, for the purpose of optimizing the annealing temperature, a series of Co$_2$Ni@NC-T catalysts were examined. It is found that the Co$_2$Ni@NC under the 800 °C treatment shows the highest OER activity (Fig. S10†).

To deeply realize the intrinsic high activity of Co$_2$Ni@NC for OER, we conducted the electrochemical active surface area (ECSA) tests. The electrochemical area of Co$_2$Ni@NC (1.38 mF cm^{-2}) examined by cyclic voltammogram (CV) (Fig. S11†) is larger than those of other samples (Fig. 4d). The larger electrochemical area is associated with more active sites at the solid–liquid interface. Besides, the electrochemical impedance spectroscopy (EIS) measurements show that the Co$_2$Ni@NC has the smallest charge transfer resistance (R_{ct} = 32.8 Ω) in comparison with other catalysts, indicating a fast electron transfer and the rapid OER kinetics at the catalyst/electrolyte interface (Fig. 4e). Additionally, we calculated the turn over frequencies (TOFs) per surface site at different potentials for these catalysts to gain an insight into the intrinsic catalytic activity. Fig. S12† shows the TOF value on the Co$_2$Ni@NC (0.043 s^{-1}) at an overpotential of 450 mV, which is about 4.1 and 6.8 times of the pure Ni@NC and Co@NC catalysts, respectively, indicating that the introduction of the Co–Ni alloy increases the OER catalytic activity of Co$_2$Ni@NC.

Apart from the outstanding OER activity, Co$_2$Ni@NC also displays an excellent long-term stability. After 1000 consecutive CV cycles at a scan rate of 100 mV s^{-1} in 1.0 M KOH, Co$_2$Ni@NC only shows a slight increase of potential (Fig. 4f). What's more,

the stable time-dependent current over 12 h further demonstrates the good stability of Co$_2$Ni@NC for OER, which should be associated with the distinctive architecture of Co–Ni alloy encapsulated in nitrogen-doped porous carbon, protecting active materials from agglomeration and pulverization. XRD and XPS characterizations were conducted to verify the catalyst composition after the durability test. The XRD pattern shows that the phase characteristic of the Co$_2$Ni@NC catalyst is not changed (Fig. S13†). In addition, from the high-resolution Co 2p and Ni 2p XPS spectra after the OER stability test, the signals of Co^{3+} (779.1 eV) and Ni^{3+} (853.7 eV) are emerged on the surface of the sample, which is beneficial for enhancing the OER activity (Fig. S14†).[13]

To further understand the relationship between Co–Ni alloy composition and OER performance, first-principles simulations based on density functional theory (DFT) were performed via Vienna $ab\ initio$ simulation package (VASP).[22–24] The calculations were made for models in a different regime of that expected for the experimental particles. As is well-known, OER follows a four-electron transfer process in alkaline environment and could be written as:

$$OH^- + * \rightarrow HO* + e^- \tag{1}$$

$$OH* + OH^- \rightarrow H_2O + O* + e^- \tag{2}$$

$$O* + OH^- \rightarrow HOO* + e^- \tag{3}$$

$$HOO* + OH^- \rightarrow O_2^* + e^- \tag{4}$$

where the * means an active site of the (111) surface, and O*, HO*, and HOO* stand for the (111) surface with adsorbed O, OH, and OOH, respectively (Fig. 5a). Finding the relationships between the free energy of different compositions and the overpotential is of great significance for the rational design of electrochemical catalysts. The free energy diagrams of the OER steps for pristine Co and modified Co–Ni model are displayed in Fig. 5b and c. The strong interactions between OH and the catalysts lead to a negative value of the ΔG_1.[41] In addition, the
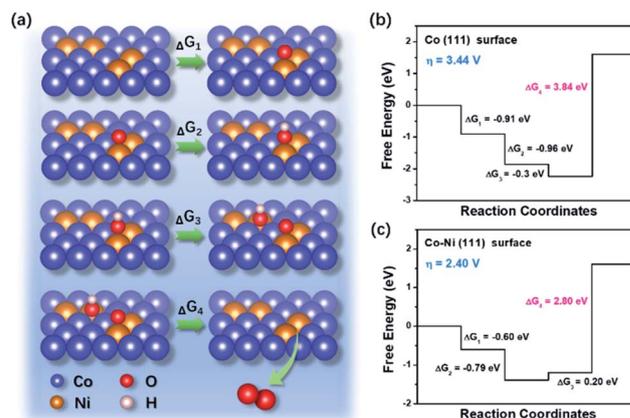

Fig. 5 (a) The schematic illustration of OER process on the Co–Ni surfaces. Free energy diagrams for the OER of (b) Co (111) and (c) Co–Ni (111) surfaces.

last steps are the rate-limiting step for these two systems. After introducing Ni, the Co–Ni model requires an overpotential of 2.40 V which is lower than 3.44 V of pristine Co, this is consistent with the experimental conclusion. Our calculated results show that the Co–Ni model can significantly reduce the activation barrier compares to its single metal counterpart. The synergistic effect between Co and Ni can effectively adjust the binding energy tending to an optimal value, further improving the energetics for the OER.

The outstanding OER activity of the $Co_2Ni@NC$ could be ascribed to the following aspects: firstly, the well-designed hierarchical structures with large surface area effectively increase the contact area between electrode and electrolyte. Second, the homogeneous CoNi alloy with an optimized component can efficiently adjust the electronic structure and significantly improve the electrocatalytic performance owing to their additional synergistic effects. Third, the *in situ* nitrogen doped carbon coating not only enhances the electrical conductivity, but also induces a charge rearrangement on the carbon materials to create new catalytic centers. What's more, the carbon coating protects active materials from agglomeration and pulverization, resulting in an improved cycling stability.

4. Conclusions

In summary, we have developed a controllable strategy to assemble the cobalt–nickel alloy nanoparticles encapsulated in nitrogen-doped porous carbon frameworks by annealing a bimetal–organic framework. Benefiting from the porous hierarchical nanostructures and component modulation, the optimized $Co_2Ni@NC$ catalyst realizes abundant synergistic active sites and fast mass transfer for OER, showing superiorly high electrocatalytic activities (310 mV, 10 mA cm^{-2}) and excellent durability in alkaline solution. The outstanding electrochemical performance along with the clear explanation of the reaction mechanism, provides a deep understanding and great prospects for the MOF-derived $Co_2Ni@NC$ as a high-performance OER electrocatalyst.

Conflicts of interest

There are no conflicts to declare.

Acknowledgements

References

1 N. Armaroli and V. Balzani, *Angew. Chem., Int. Ed.*, 2007, **46**, 52–66.

2 M. S. Dresselhaus and I. L. Thomas, *Nature*, 2001, **414**, 332–337.

3 S. Chu and A. Majumdar, *Nature*, 2012, **488**, 294–303.

4 C. Wang, J. Jiang, T. Ding, G. Chen, W. Xu and Q. Yang, *Adv. Mater. Interfaces*, 2016, **3**, 1500454.

5 M. Pramanik, C. Li, M. Imura, V. Malgras, Y. M. Kang and Y. Yamauchi, *Small*, 2016, **12**, 1709.

6 K. C. Neyerlin, G. Bugosh, R. Forgie, Z. Liu and P. Strasser, *J. Electrochem. Soc.*, 2009, **156**, 363–369.

7 T. Reier, M. Oezaslan and P. Strasser, *ACS Catal.*, 2012, **2**, 1765–1772.

8 Y. Hou, M. R. Lohe, J. Zhang, S. H. Liu, X. D. Zhuang and X. L. Feng, *Energy Environ. Sci.*, 2016, **9**, 478–483.

9 Y. Yang, Z. Y. Lin, S. Q. Gao, J. W. Su, Z. Y. Lun, G. L. Xia, J. T. Chen, R. R. Zhang and Q. W. Chen, *ACS Catal.*, 2017, **7**, 469–479.

10 M. Li, T. T. Liu, X. J. Bo, M. Zhou and L. P. Guo, *J. Mater. Chem. A*, 2017, **5**, 5413–5425.

11 X. Zhang, H. Xu, X. Li, Y. Li, T. Yang and Y. Liang, *ACS Catal.*, 2016, **6**, 580–588.

12 W. J. Wan, X. J. Liu, H. Y. Li, X. Y. Peng, D. S. Xi and J. Luo, *Appl. Catal., B*, 2019, **240**, 193–200.

13 Y. Fu, H. Y. Yu, C. Jiang, T. H. Zhang, R. Zhan, X. W. Li, J. F. Li, J. H. Tian and R. Z. Yang, *Adv. Funct. Mater.*, 2018, 1705094.

14 L. T. Yan, L. Cao, P. C. Dai, X. Gu, D. D. Liu, L. J. Li, Y. Wang and X. B. Zhao, *Adv. Funct. Mater.*, 2017, 1703455.

15 N. N. Du, C. M. Wang, X. J. Wang, Y. Lin, J. Jiang and Y. J. Xiong, *Adv. Mater.*, 2016, **28**, 2077–2084.

16 X. B. Liu, Y. C. Liu and L. Z. Fan, *J. Mater. Chem. A*, 2017, **5**, 15310–15314.

17 Y. Xu, W. G. Tu, B. W. Zhang, S. M. Yin, Y. Z. Huang, M. Kraft and R. Xu, *Adv. Mater.*, 2017, **29**, 1605957.

18 Y. D. Ma, X. P. Dai, M. Z. Liu, J. X. Yong, H. Y. Qiao, A. X. Jin, Z. Z. Li, X. L. Huang, H. Wang and X. Zhang, *ACS Appl. Mater. Interfaces*, 2016, **8**, 34396–34404.

19 Y. Z. Chen, C. M. Wang, Z. Y. Wu, Y. J. Xiong, Q. Xu, S. H. Yu and H. L. Jiang, *Adv. Mater.*, 2015, **27**, 5010–5016.

20 G. Kresse and D. Joubert, *Phys. Rev. B*, 1999, **59**, 1758–1775.

21 J. P. Perdew, K. Burke and M. Ernzerhof, *Phys. Rev. Lett.*, 1996, **77**, 3865–3868.

22 G. Kresse and J. Hafner, *Phys. Rev. B*, 1993, **47**, 558–5611.

23 G. Kresse and J. Furthmüller, *Phys. Rev. B*, 1996, **54**, 11169–11186.

24 G. Kresse and J. Furthmüller, *Comput. Mater. Sci.*, 1996, **6**, 15–50.

25 S. Grimme, S. Ehrlich and L. Goerigk, *J. Comput. Chem.*, 2011, **32**, 1456–1465.

26 J. K. Nørskov, J. Rossmeisl, A. Logadottir, L. Lindqvist, J. R. Kitchin, T. Bligaard and H. Jonsson, *J. Phys. Chem. B*, 2004, **108**, 17886–17892.

27 I. C. Man, H. Y. Su, F. Calle-Vallejo, H. A. Hansen, J. I. Martínez, N. G. Inoglu, J. Kitchin, T. F. Jaramillo, J. K. Nørskov and J. Rossmeisl, *ChemCatChem*, 2011, **3**, 1159–1165.

28 A. Abbasi, M. Soleimani, M. Najafi and S. Geranmayeh, *J. Mol. Struct.*, 2017, **1133**, 458–463.

29 X. F. Xiao, C. T. He, S. L. Zhao, J. Li, W. S. Lin, Z. K. Yuan, Q. Zhang, S. Y. Wang, L. M. Dai and D. S. Yu, *Energy Environ. Sci.*, 2017, **10**, 893–899.

30 Y. Hou, S. M. Cui, Z. H. Wen, X. R. Guo, X. L. Feng and J. H. Chen, *Small*, 2015, **44**, 5940–5948.

31 X. T. Yuan, M. S. Riaz, X. Wang, C. L. Dong, Z. Zhang and F. Q. Huang, *Chem.–Eur. J.*, 2018, **24**, 3707–3711.

32 Z. H. Xue, H. Su, Q. Y. Yu, B. Zhang, H. H. Wang, X. H. Li and J. S. Chen, *Adv. Energy Mater.*, 2017, **7**, 1602355.

33 Y. X. Zhang, L. Sun, L. Q. Bai, H. C. Si, Y. Zhang and Y. H. Zhang, *Nano Res.*, 2019, **12**, 607–618.

34 J. S. Zhang, C. X. Wu, M. H. Huang, Y. Zhao, J. X. Li and L. H. Guan, *ChemCatChem*, 2018, **10**, 1336–1343.

35 S. L. Yang, T. R. Zhang, G. C. Li, L. Q. Yang and J. Y. Lee, *Energy Storage Mater.*, 2017, **6**, 140–148.

36 X. G. Feng, X. J. Bo and L. P. Guo, *J. Power Sources*, 2018, **389**, 249–259.

37 Y. Li, H. X. Li, K. Z. Cao, T. Jin, X. J. Wang, H. M. Sun, J. X. Ning, Y. J. Wang and L. F. Jiao, *Energy Storage Mater.*, 2018, **12**, 44–53.

38 W. P. Kang, Y. Zhang, L. L. Fan, L. L. Zhang, F. N. Dai, R. M. Wang and D. F. Sun, *ACS Appl. Mater. Interfaces*, 2017, **9**, 10602–10609.

39 X. F. Lu, L. F. Gu, J. W. Wang, J. X. Wu, P. Q. Liao and G. R. Li, *Adv. Mater.*, 2017, **29**, 1604437.

40 Z. Q. Zhu, F. Y. Cheng and J. Chen, *J. Mater. Chem. A*, 2013, **1**, 9484–9490.

41 X. Zhang, A. Chen, Z. H. Zhang, M. G. Jiao and Z. Zhou, *J. Mater. Chem. A*, 2018, **6**, 11446–11452.